Journal of Controlled Release 245 (2017) 52–61

Contents lists available at ScienceDirect

Journal of Controlled Release

journal homepage: www.elsevier.com/locate/jconrel

Multifunctional gold-nanoparticles: A nanovectorization tool for the targeted delivery of novel chemotherapeutic agents

Alexandra R. Fernandes [a,b,*], João Jesus [a], Pedro Martins [a], Sara Figueiredo [a], Daniela Rosa [a], Luísa M.R.D.R.S. Martins [b,c], Maria Luísa Corvo [d], Manuela C. Carvalheiro [d], Pedro M. Costa [e], Pedro V. Baptista [a,**]

[a] UCIBIO, Departamento Ciências da Vida, Faculdade de Ciências e Tecnologia, Campus de Caparica, Universidade Nova de Lisboa, 2829-516 Caparica, Portugal
[b] CQE, Centro de Química Estrutural, Instituto Superior Técnico, Universidade de Lisboa, Av Rovisco Pais, 1049-001 Lisboa, Portugal
[c] Área Departamental de Engenharia Química, Instituto Superior de Engenharia de Lisboa, R. Conselheiro Emídio Navarro, 1959-007 Lisboa, Portugal
[d] Instituto de Investigação do Medicamento (iMed.ULisboa), Faculdade de Farmácia, Universidade de Lisboa, Av. Prof. Gama Pinto, 1649-003 Lisboa, Portugal
[e] MARE - Marine and Environmental Sciences Centre, Departamento de Ciências e Engenharia do Ambiente, Faculdade de Ciências e Tecnologia, Universidade Nova de Lisboa, 2829-516 Caparica, Portugal

ARTICLE INFO

Article history:
Received 21 July 2016
Received in revised form 4 November 2016
Accepted 17 November 2016
Available online 18 November 2016

Keywords:
Gold nanoparticles
Targeting
Nanomedicine
Cancer therapy
Metal complexes
Colorectal cancer
Lung cancer

ABSTRACT

Due to their small size and unique properties, multifunctional nanoparticles arise as versatile delivery systems easily grafted with a vast array of functional moieties, such as anticancer cytotoxic chemotherapeutics and targeting agents. Here, we formulated a multifunctional gold-nanoparticle (AuNP) system composed of a monoclonal antibody against epidermal growth factor receptor (EGFR) (anti-EGFR D-11) for active targeting and a Co(II) coordination compound $[CoCl(H_2O)(phendione)_2][BF_4]$ (phendione = 1,10-phenanthroline-5,6-dione) (TS265) with proven antiproliferative activity towards cancer cells (designated as TargetNanoTS265). The efficacy of this nanoformulation, and the non-targeted counterpart (NanoTS265), were evaluated in vitro using cancer cell models and in vivo using mice xenografts. Compared to the free compound, both nanoformulations (TargetNanoTS265 and NanoTS265) efficiently delivered the cytotoxic cargo in a controlled selective manner due to the active targeting, boosting tumor cytotoxicity. Treatment of HCT116-derived xenografts tumors with TargetNanoTS265 led to 93% tumor reduction. This simple conceptual nanoformulation demonstrates the potential of nanovectorization of chemotherapeutics via simple assembly onto AuNPs of BSA/HAS-drug conjugates that may easily be expanded to suit other cargo of novel compounds that require optimized controlled delivery to cancer target.

1. Introduction

The development of AuNPs is at the core of many of these recent innovative systems, as multifunctional scaffolds capable to integrate diagnosis, drug monitoring, targeted delivery, and controlled drug release functions into a single platform [1,2]. In recent years the growing focus of oncology onto targeted therapies has placed AuNPs as attractive candidates for the delivery of drug payloads directly into cancer cells due to its physicochemical properties including relatively high biocompatibility and ease conjugation to biomolecules, capable of improving drug delivery and increased targeting efficacy [3–8]. Indeed, AuNPs have been effectively used to deliver i) drugs and contrast agents that otherwise exhibit low solubility and poor pharmacokinetics and ii) compounds that are naturally susceptible to enzymatic degradation, as well as those that display low intracellular penetration (e.g. siRNA) [8,9]. These AuNP based systems may be of the utmost importance to overcome current limitations in cancer therapy, such as side effects and acquisition of multidrug resistance [10]. Our group pioneered the use of AuNPs functionalized with hairpin ssDNA structures labeled with a fluorophore - gold nanobeacon (Au-nanobeacon) – to effectively silence any possible RNA mediated pathway inside the cell with low toxicity [11,12]. This system was shown to be effective in vivo in a promising approach to combat multidrug resistant tumors, combining in the same particle an antitumor agent (5-fluorouracil) with silencing of *MRP1*, a gene associated with acquired resistance in several tumors. In vivo results showed a remarkable tumor size reduction, from the synergic effect of the two agents [13]. AuNPs can be surface functionalized with active ligands at high densities (100× higher than that attainable with conventional liposomes) [14]. By capitalizing on the receptor-ligand

* Co-corresponding author: A. R. Fernandes, UCIBIO, Departamento de Ciências da Vida, Faculdade de Ciências e Tecnologia, Universidade Nova de Lisboa, Campus de Caparica, 2829-516 Caparica, Portugal.
** Corresponding author: Pedro Viana Baptista, UCIBIO, Departamento de Ciências da Vida, Faculdade de Ciências e Tecnologia, Universidade Nova de Lisboa, Campus de Caparica, 2829-516 Caparica, Portugal.
E-mail addresses: ma.fernandes@fct.unl.pt (A.R. Fernandes), pmvb@fct.unl.pt (P.V. Baptista).

http://dx.doi.org/10.1016/j.jconrel.2016.11.021
0168-3659/

molecular interaction, AuNPs drug payload and other therapeutic molecules have been described to be internalized into the cells by receptor-mediated endocytosis [15–17]. Nevertheless, the cell type and the nanoparticles´physicochemical properties (e.g. size, shape, or surface functionalities) can affect the internalization mechanism [18,19] and depending on the mechanisms that cells use to internalize the nanoparticles, its compartmentalization may vary, as does its biological fate and the release of the drug [20]. Among the several documented molecular alterations present at the surface of cancer cells, the increase expression of the epidermal growth factor receptor (EGFR) is well documented regarding cancer treatment, and may be targeted using a monoclonal antibody such as anti-EGFR D-11 [20,21].

The Co(II) coordination compound $CoCl(H_2O)(phendione)_2][BF_4]$ (phendione = 1,10-phenanthroline-5,6-dione) – TS265, shows high cytotoxic effect against cancer cell lines particularly colorectal and hepatocellular carcinoma cell lines and a much lower cytotoxicity towards normal human fibroblasts [22]. We have previously demonstrated that TS265 induces cell cycle arrest in S phase with subsequent cell death by apoptosis, via the promotion of the upregulation of pro-apoptotic Bax and cell-cycle-related p21; reduces expression of proteins typically upregulated in tumors and is able to produce double-strand breaks in a concentration-dependent manner. Steady-state and time-resolved fluorescence spectroscopy studies demonstrated a strong and specific interaction of the complex with human serum albumin (HSA), suggesting that this complex can be efficiently transported by albumin in the blood plasma [22–24]. The higher cytotoxicity towards HCT116 tumor cells compared with normal human fibroblasts prompt us to further enhance its cytotoxic potential by using gold nanoparticles as multifunctional nanovectorization system.

Here, we have designed a conceptual nanovectorization tool for targeted chemotherapy using TS265 as a model drug. The conceptual design of the multifunctional nanovectors involves the synthesis of ~14 nm AuNPs readily functionalized with bifunctional PEG (SH-EG(8)-(CH2)2-COOH) to provide for stability and stealth capability in vivo, bovine serum albumin (BSA) to convey TS265 (due to the previous knowledge that TS265 interacts with albumin [24]) and the anti-EGFR D-11 monoclonal antibody as a targeting moiety towards cancer cells (due to the high expression of EGFR in cancer cells [20,21]). The novel nanoformulation (TargetNanoTS265) was evaluated in NSCLC cell lines, colorectal cancer cell lines and immunocompromised mice in order to understand its targeting and therapeutic potential.

2. Experimental section

2.1. Compounds

The metal compound $[Co(Phendione)_2(H_2O)Cl]BF_4]$ (TS265) was synthesized and characterized as previously described [22]. Paclitaxel (PTX) was purchased from Sigma-Aldrich (Spain). Millipore® water was used for the preparation of all aqueous solutions. Human Serum albumin (HSA, 96–99% with a molecular mass of 66–67 kDa) and Bovine Serum Albumin (BSA, 98% with a molecular mass of 66 kDa) were purchased from Sigma-Aldrich.

2.2. Interaction studies of TS265 with albumin

HSA and BSA stock solutions were prepared by gently dissolving the protein in phosphate buffer pH 7.0 with 0.15 M NaCl, gently swirled for 45 min to allow the protein to hydrate and fully dissolve. The concentration of each stock solution was determined by UV spectrophotometry using the molar extinction coefficient at 278 nm (HSA = 36.850 M^{-1} cm^{-1} and BSA = 43.824 M^{-1} cm^{-1}) [24]. Spectroscopic and UV-VIS measurements were carried out on individually prepared samples to ensure the same pre-incubation time at (37.0 ± 0.5) °C in each essay. For Spectroscopic measurements HSA and BSA concentrations were kept constant at 2.0 μM and 0.13 μM, respectively, while the concentration of the complex ranged from 0 to 375 μM. For UV–VIS measurements BSA concentration was kept constant at 2.0 μM, while the concentration of the TS265 complex ranged from 0 to 60 μM. Samples were incubated at 37 °C for 1 h.

2.3. Spectroscopic measurements

UV–Visible absorption spectra were recorded at room temperature on a UV–VIS spectrophotometer (UVmini 1240, Shimadzu, Germany) in the range 230–500 nm with 1 cm path quartz Suprasil® cuvettes as described previously [22,24]. Fluorescence measurements were carried out on a Cary Eclipse Fluorescence spectrophotometer (Agilent Technologies, Spain) at room temperature as described previously [24].

2.4. Cell culture

A549 (ATCC® CCL-185™) and HCT116 (ATCC® CCL-247™) tumor cell lines obtained from ATCC (Chicago, IL) were grown in Dulbecco's Modified Eagle Medium (DMEM; Invitrogen, New York, EUA) and supplemented with 10% (v/v) Fetal Bovine Serum (FBS, Invitrogen) and 1% (v/v) antibiotic/antimycotic (Invitrogen, New York, EUA). NCI-H1975 [H-1975, H1975] (ATCC® CRL-5908™) human lung adenocarcinoma cells were grown in RPMI (Roswell Park Memorial Institute) 1640 medium (RPMI; Invitrogen, New York, EUA) supplemented with 10% (v/v) FBS and 1% (v/v) antibiotic/antimycotic solution (Invitrogen). Cells were maintained in 75 cm^2 culture flasks (VWR) at 37 °C in a 99% humidified atmosphere of 5% (v/v) CO_2 (CO_2 Incubator Leec, UK). Primary human fibroblasts were cultured as previously described [22].

2.5. Gold nanoparticles synthesis and assembly of Au-nanoconjugates

AuNPs were synthesized by the citrate reduction method described by Lee and Meisel [25] and characterized by UV–VIS spectroscopy, Transmission electron microscopy (TEM) and dynamic light scattering (DLS). AuNPs functionalization with PEG (AuNP@PEG) was performed following incubation the AuNPs solution (10 nM) with 0.028% (w/v) Sodium dodecyl sulfate (SDS), and SH-EG(8)-(CH2)2-COOH (Iris-Biotech) for a period of 16 h under agitation at room temperature. The excess of PEG chains was removed by centrifugation at 14000 g for 30 min at 4 °C and the degree of PEG coverage on the AuNPs' surface evaluated via Ellman's Assay [9,12].

AuNP@PEG were functionalized with Human Serum Albumin (HSA) (AuNP@PEG@HSA) or Bovine Serum Albumin (BSA) (AuNP@PEG@BSA) (Sigma, MW 66,120 kDa) by a process based on a EDC/NHS reaction. Briefly, a master mix of 21 nM of the synthesized AuNP@PEG, 1.25 mg/mL sulfo-NHS (Sigma, MW 217.13 Da) and 0.312 mg/mL EDC (Sigma, MW 191.70 Da) in 10 mM pH 6 MES buffer (2-(N-morpholino)ethanesulfonic acid) (Sigma, MW 195.24 Da). The master mix was incubated for 30 min and then centrifuged at 14000 g for 30 min at 4 °C. The supernatant was removed and replaced by 2.5 mM pH 6 MES buffer. The master mix was incubated with

10 μg/mL of BSA or HSA for 16 h. Afterwards the suspensions were washed twice with MES buffer to remove the excess BSA/HSA, through centrifugation at 14000 g for 30 min at 4 °C. Supernatants were also recovered and tested for protein concentration using Bradford Assay (Thermo Scientific). AuNP@PEG were also functionalized with *anti*-EGFR D-11 (Santa Cruz Biotechnology, USA) and with the same BSA concentration 1 h prior to antibody addition (AuNP@PEG@anti-EGFR_BSA) under the previously described conditions. Anti-EGFR D-11 antibody was added to reaction mix at a final concentration of 33 μg/mL. Subsequently, 6 nM AuNP@PEG@BSA, 6 nM AuNP@PEG@HSA and 6 nM AuNP@PEG@anti-EGFR_BSA were mixed separately with 50 μM of TS265 and incubated for 1 h at 4 °C to obtain AuNP@PEG@BSA@TS265, AuNP@PEG@HSA-TS265, AuNP@PEG@anti-EGFR_BSA@TS265, respectively. After this period, solutions were centrifuged at 14000 g for 30 min at 4 °C, to remove excess of TS265. The amount of TS265 in the

supernatants was quantified by Inductively Coupled Plasma mass spectrometry (ICP-MS).

AuNP@PEG@BSA were also functionalized with 50 μM PTX and incubated for 1 h at 4 °C to obtain AuNP@PEG@BSA@PTX (NanoPTX). After this period, solutions were centrifuged at 14000 g for 30 min at 4 °C, to remove excess of PTX. The amount of PTX in the supernatant was quantified by UV–Vis spectroscopy.

The nanoconjugates' hydrodynamic diameter was determined by DLS with a Nanoparticle Analyzer SZ-100 (Horiba Scientific, Japan) at 25 °C, with a scattering angle of 90°. The AuNP formulations were diluted in milli-Q water to a final concentration of 2 nM prior to analysis. A total of 3 measurements were performed for each sample. For TEM analysis samples were prepared by depositing 10 μL of the gold colloidal solution in carbon copper grids, washing twice with milli-Q water, and air

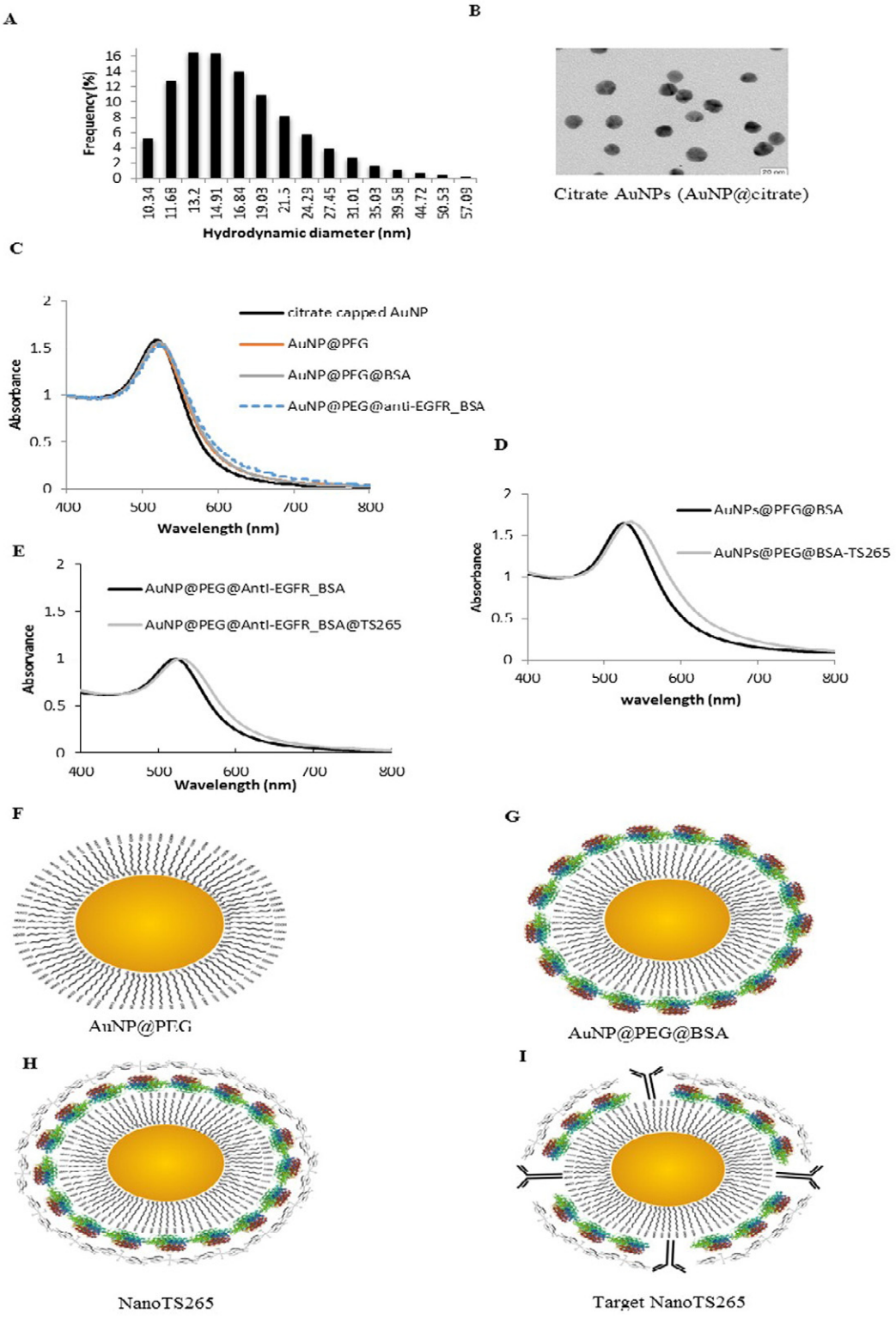

Fig. 1. Nanoconjugate characterization: A) citrate capped AuNPs hydrodynamic diameter; B) TEM image from citrate capped AuNPs; C), D) and E) UV–VIS spectroscopy of the different AuNPs nanoconjugates (AuNP@PEG, AuNP@PEG@BSA, NanoTS265 and TargetNanoTS265); F), G), H) and I) schematic representation of AuNPs nanoconjugates used in this study.

dried. The service was provided by Instituto de Ciência e Engenharia de Materiais e Superfícies at Instituto Superior Técnico (ICEMS/IST), Portugal.

2.6. Cell viability assessment by the MTS assay

HCT116, A549 and H1975 cells were seeded at a density of 7.5×10^4/well in 96-well plates and grown for 24 h prior to incubation for 24 or 48 h in fresh diluted medium with and without the nanoconjugates or free TS265 or PTX (37 °C in a 99% humidified atmosphere of 5% (v/v) CO_2). Each nanoconjugates' concentration was determined so as to match the equivalent number of molecules of free TS265 or PTX. The IC_{50} was determined for the free TS265 in A549 and H1975 as previously described for HCT116 cells [22]. IC_{50} was also determined for the free PTX. Standard MTS reduction assay - CellTiter 96® AQueous non-radioactive cell proliferation assay (Promega, Madison, WI, USA) was used after 24 h and 48 h incubation periods to determine cell viability. Briefly, culture medium was removed from each well, washed with PBS, and replaced with 100 μL of complete MTS solution (100:20:1 ratio of cell culture medium, MTS and PMS, respectively). The 96 well plate was incubated for 30 min at 37 °C in a 99% humidified atmosphere of 5% v/v) CO_2 and the absorbance was measured directly from 96 well plates in a microplate reader at 490 nm (Infinite M200, Tecan, Switzerland). The percentage of cell viability for each concentration was determined taking into account three independent assays.

3. Internalization of the nanoconjugates

In order to quantify nanoconjugate internalization, with and without TS265, the amount of Au and Co in the supernatants and in pelleted cells was quantified by ICP-MS. Briefly, HCT116 cells were seeded at a density of 3.75×10^5/well in 24-well plates and grown for 24 h prior to incubation for an additional 24 h in fresh diluted medium with and without the nanoconjugates (37 °C in a 99% humidified atmosphere of 5% (v/v) CO_2). Each nanoconjugate concentration was determined to match the equivalent number of molecules of free TS265 used in cell viability assays. After 24 h incubation, the supernatants were removed and diluted in aqua regia, and the cells were tripsinized, recovered and diluted in aqua regia. These aqua regia solutions were then assayed by ICP-MS. Assays were performed in triplicate.

4. Hoechst 33258 labelling

HCT116 Cells were plated in 35 mm dishes at 150,000 cells/dish. Culture medium was removed 24 h after platting and replaced with 2 mL of fresh medium containing free TS265 (at IC_{50}), NanoTS265 (TS265 at IC_{50}), free TS265 (at IC_{25}), NanoTS265 (TS265 at IC_{25}) or water (vehicle control). Cells were stained after an incubation period of 48 h. Hoechst staining assay was performed as described in [23]. Plates were photographed in an AXIO Scope (Carl Zeiss, Oberkochen Germany). Images are representative of at least three independent experiments.

4.1. Selectivity assay

HCT116 human colorectal carcinoma cell line and human primary fibroblasts were seeded at a cell density of 1×10^5 cell/well (1:1 ratio) over a cover slip within a 24-well plate well for 24 h, and then incubated with nanoconjugates for a further 6 h. Cells were fixed with 4% paraformaldehyde for 10 min at room temperature and permeabilized with 0.1% Triton X-100 for 5 min. Cells were double stained with anti-Vimentin 1:200 (Sigma-Aldrich) for 1 h and anti-mouse TRITC 1:64 (Sigma) for 30 min, and with Phalloidin 488 Alexa Fluor 3:200 (Invitrogen, Life Technologies, USA) for 20 min. Glass slides were mounted in ProLong® Gold Antifade Reagent with DAPI (Invitrogen, LifeTechnologies, USA) to allow for nuclear staining. Co-culture immunofluorescent images of HCT116 cell line and fibroblasts primary cell culture were acquired with a Zeiss Axioplan 2 Imaging Microscope and a Nikon DXM1200F digital camera.

4.2. In vivo assay

All animal experiments were carried with the permission of the Portuguese Authority (Direcção Geral de Alimentação e Veterinária) and the study was approved by the Local Ethical Committee (Comissão de Ética Experimentação Animal da Faculdade de Farmácia, Universidade de Lisboa), and in accordance with the Declaration of Helsinki, the EEC Directive (2010/63/UE) and Portuguese law (DL 113/2013, Despacho no 2880/2015), and all following legislations for the humane care of animals in research. Animals were kept under sterilized conditions using an Air Handling Easy Flow Ventilation Unit with single-sided racks and Blue Line NEXT individually ventilated cages (Tecniplast, Italy). Animals were fed with sterilized commercial chow, and given sterilized

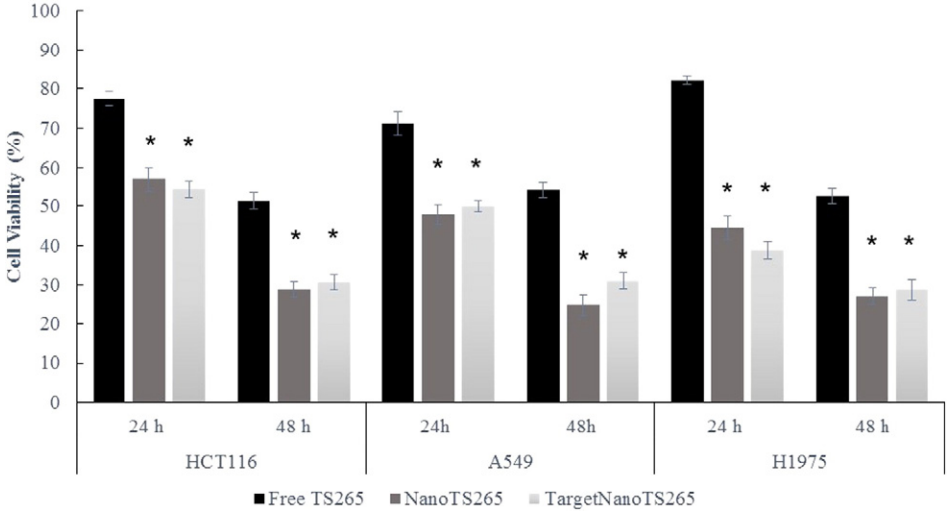

Fig. 2. Cell viability after 24 h and 48 h exposure to the nanoconjugates and the free TS265 (concentration equivalent to IC_{50} at 48 h) in HCT116, A549 and H1975 tumor cell lines. Percentage of cell viability for each concentration was calculated relative to the control cells and is the mean of three independent assays (error bars correspond to SEM). See also Supplementary material Fig. S7 for nanoconjugates alone. *$p < 0.0001$ relative to each free TS265.

Table 1
Reduction of cell viability (%) due to the exposure of HCT116, A549 and H1975 tumor cell lines to the nanoconjugates or the free TS265.

Cell line	Time (h)	NanoTS265	TargetNanoTS265	Free TS265
HCT116	24	43.2 ± 3.3	45.7 ± 4.1	22.5 ± 1.8
	48	71.1 ± 2.6	69.2 ± 2.9	48.7 ± 5.6
A549	24	52.2 ± 1.2	50.0 ± 2.3	28.8 ± 2.6
	48	75.2 ± 2.0	68.9 ± 1.0	46.0 ± 2.0
H1975	24	55.6 ± 2.7	61.2 ± 3.0	17.9 ± 2.0
	48	72.8 ± 2.1	71.1 ± 2.2	47.5 ± 2.6

water *ad libitum*. Adequate measures were taken in order to minimize stress, pain or discomfort of the animals.

5. Therapeutic activity study - induction/measurements

A group of 18 (3 for each experimental condition) Non-Obese Severe Combined Immunodeficient (NOD/SCID) male mice (Instituto Gulbenkian de Ciência) with 13 week old has been used. HCT116-derived xenografts were induced by s.c. administration of 1×10^6 cells at the back hip of mice. Tumors were allowed to grow until the size of 1 mm^3 and treatments were initially performed with one i.v. injection in the tail vein with the free TS265 and the four nanoconjugates (AuNP@PEG, AuNP@PEG@BSA@PEG, TargetNanoTS265 and NanoPTX) at 9.3×10^{-3} μg/kg of mice of TS265 (free or in the AuNP conjugates); and at 1.9×10^{-04} μg/kg of mice for paclitaxel (NanoPTX). A non-treated group (injected with 0.9% saline solution) was included. A second administration was performed four days after the first injection at identical doses. Tumor volume was determined three times a week by measuring with calipers in two dimensions and the tumor volume (V) was estimated using the eq. $V = (\text{length}) \times (\text{width})^2 / 2$. Mice were monitored routinely for physical status. Mice were sacrificed 5 days after the last treatment.

6. Samples

At the end of the experience mice were anesthetized with Isoflurane (Isoflo, Esteve Farma), and blood was collected by puncture from the orbital cavity. Animals were sacrificed by neck hyperextension and organs of interest (brain, spleen, kidneys and livers) and tumor were extracted weighted, washed with cold 0.154 M KCl to remove the excess blood and divided in two pieces: one for ICP-MS quantification of gold and cobalt, and the other for histological studies.

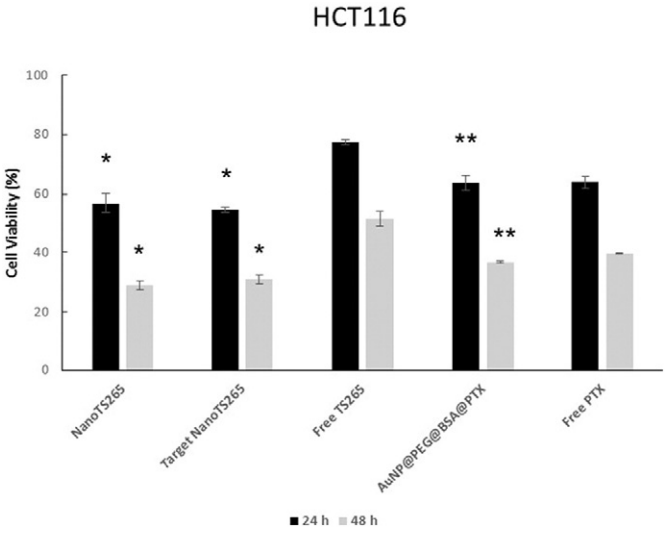

Fig. 4. HCT116 cell viability after exposure to the nanoconjugates NanoTS265, TargetNanoTS265, NanoPTX or free TS265 or free PTX (at concentrations equivalent to the IC_{50} of both compounds). Percentage of cell viability for each concentration is relative to the mean of three independent assays and error bars correspond to SEM. $^*p < 0.0001$ relative to free TS265; $^{**}p < 0.001$ relative to free PTX. NanoTS265 and TargetNanoTS265 were compared to free TS265 and NanoPTX to free PTX.

7. Histological studies

Samples of liver and tumor were carefully excised fresh and immediately fixed in 10% (v/v) neutral-buffered Formalin solution (Sigma-Aldrich, USA) for 24 h. The samples were then washed, dehydrated in a progressive series of ethanol, intermediately infiltrated with xylenes and embedded in paraplast. Sections (5 μm thick) were obtained with a Jung RM 2035 microtome (Leica Microsystems). Tumors were stained

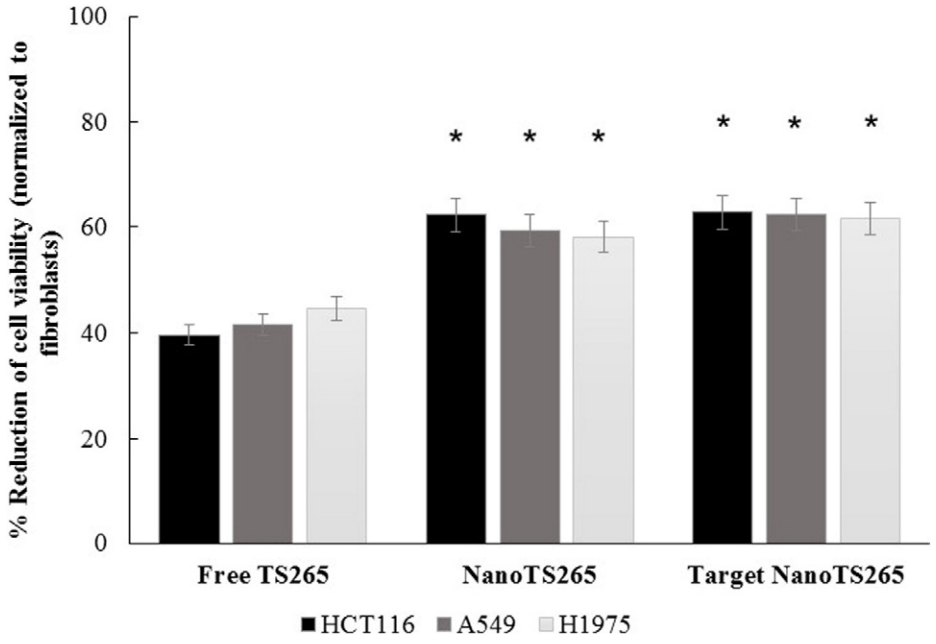

Fig. 3. Cell viability after 48 h exposure of human normal Fibroblasts and tumor cell lines (HCT116, H1975 and A549) to nanoconjugated or free TS265 (concentrations equivalent to the IC_{50} for each tumor cell line). Percentage of reduction of cell viability has been normalized to fibroblasts and is relative to the mean of three independent assays (error bars indicate SEM). $^*p < 0.001$ relative to free TS265 for each cell line.

with a tetrachrome stain (TC) for fibers and nuclei that include Alcian Blue, Weigert's Iron Hematoxylin and van Gieson's dye [26]. Liver sections were stained with Gill's Alum Hematoxylin and counterstained with alcoholic Eosin Y (H&E). Sections for the detection of metallic deposits were stained with Neutral Red only to enhance contrast, - metallic deposits, such as cobalt, are brown-blackish; while agglomerates of fine gold are purplish. All sections were dehydrated in ethanol, cleared in xylene and mounted with DPX Mountant (Sigma-Aldrich, Portugal). Observations were made with a DMLB model microscope equipped with a DFC480 digital camera (all from Leica Microsystems).

8. Statistical analysis

MTS statistical analysis was performed using GraphPad Prism v6.01. All other statistical analyses were performed using Statistical Package for the Social Sciences software v17.0 (SPSS v17.0, Chicago, IL) using the Mann–Whitney–Wilcoxon test. All data expressed as mean ± SEM from at least three independent experiments. Statistical significance was considered when p-value < 0.05.

9. Results and discussion

Stable colloidal AuNPs with an average diameter of 14 nm were synthesized with an absorption peak at 518 nm and subsequently functionalized with PEG to saturate the AuNPs surface (Fig. 1A, B and C). Functionalization with SH-PEG-COOH, increases stability and biocompatibility of AuNPs, as well granting anchoring moieties, through the carboxyl group, allowing covalent binding of amine-containing molecules, such as HSA, BSA and anti-EGFR. Upon PEG functionalization the plasmon absorption peak shifts from 518 nm to 520 nm (Fig. 1C and Supplementary material Table S1) confirming the covalent binding between AuNPs and PEG chains.

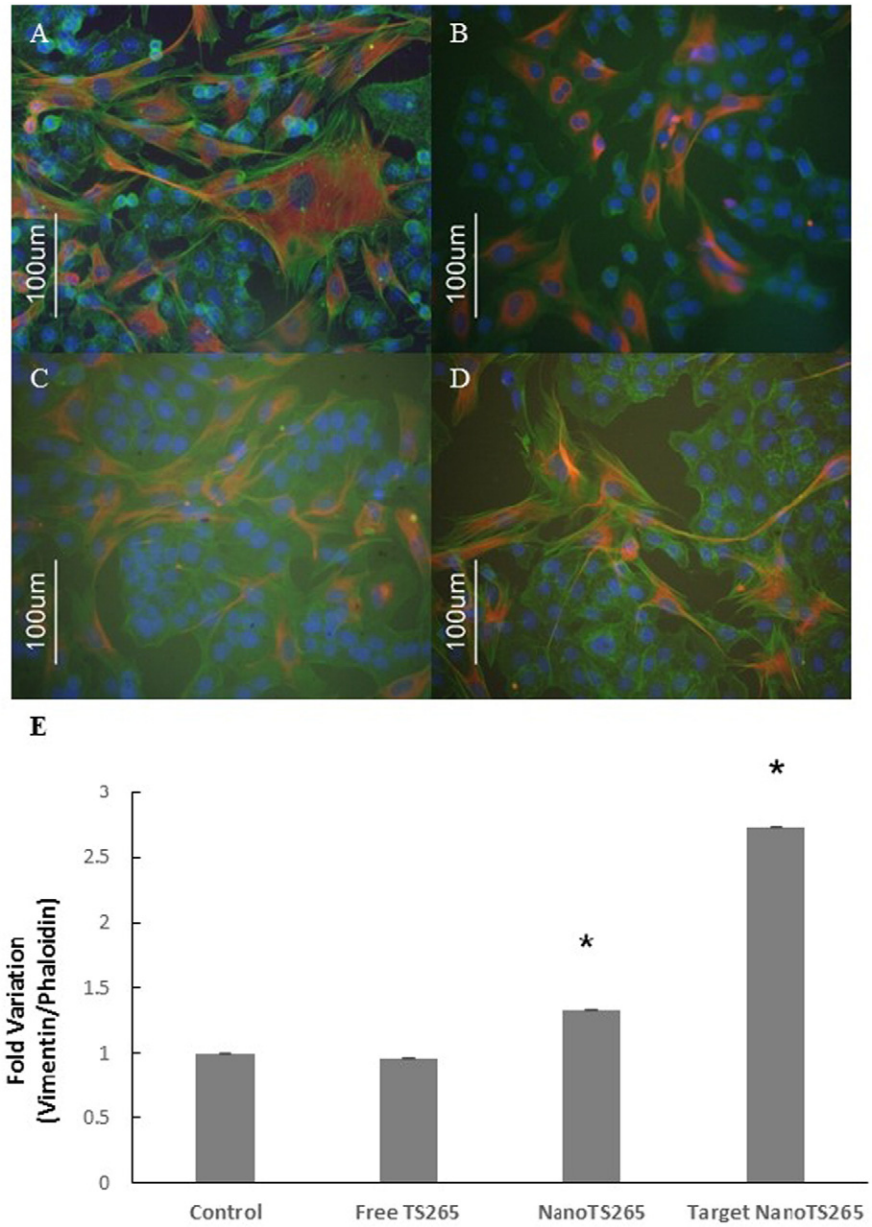

Fig. 5. Fluorescence microscopy of co-culture plates containing primary fibroblasts and HCT116 tumor cell line in a 1:1 ratio. Nucleus are stained with DAPI (blue), F-actin stained with Alexa Fluor 488 Phalloidin (green) and Vimentin stained with TRITC (red) (only expressed in fibroblasts). (A) Control, (B) free TS265, (C) NanoTS265, (D) TargetNanoTS265 and (E) anti-Vimentin: Phalloidin fluorescence fold variation. * p < 0.05 relative to control.

We have previous demonstrated the strong interaction of TS265 with HSA [24], nevertheless, taking advantage of the intrinsic fluorescence of BSA, due to two tryptophan residues, Trp-134 and Trp-212, the fluorescence quenching at various concentrations of TS265 was also studied (Supplementary material Fig. S1). As the TS265 concentration increases the BSA fluorescence intensity decreases confirming the interaction between the compound and BSA (Supplementary material Fig. S1). The interaction between TS265 and BSA is perceived via the analysis of UV–Vis spectra (Supplementary material Fig. S2), where the BSA peak at 278 nm increases with increasing TS265 concentration. No apparent blue/red shift in their maximum absorption wavelength is observed. These results indicate that the microenvironment of tryptophan residues on BSA is altered and the peptide strand is less extended with the addition of TS265. Generally, small molecules are bound to biological macromolecules by a combination of forces, which include hydrogen bond, van der-Waals, electrostatic, and hydrophobic interaction forces [27]. The observed hyperchromism confirms the non-intercalative mode of binding of TS265 to BSA and indicates that TS265 may be bound to the hydrophobic pocket (Trp-212 residue). Nevertheless, an interaction between Trp-134 and TS265 or other electrostatic interactions cannot be ruled out.

Further functionalization with BSA and HSA originated two conjugates, AuNP@PEG@BSA and AuNP@PEG@HSA whose characteristics are shown in Fig. 1C and Supplementary material Fig. S2 and Table S1. The AuNPs' plasmon absorption peak upon BSA and HSA functionalization shifts from 520 nm to 523 nm and 525 nm, respectively (Fig. 1C and Supplementary material Table S1) confirming the binding between AuNP@PEG and BSA/HSA. The determined average number of grafted molecules per AuNP was 2081 ± 157 for PEG, 7–8 for BSA and 11 for HSA (Supplementary Table S2). BSA and HSA are bound to the AuNP via covalent binding between amine groups present in both proteins and the PEG carboxyl group, which then allows loading with the desired chemotherapeutics - here TS265 and PTX as models.

Two different nanoconjugates loaded with TS265 were prepared using either BSA (NanoTS265) or AuNP@PEG@HSA-TS265 whose characteristics are depicted in Fig. 1C, Supplementary material Fig. S2, Supplementary material Tables S1 and S3. The plasmon absorption peak upon TS265 functionalization shifts from 523 to 535 nm and 525 to 532 nm in NanoTS265 and AuNP@PEG@HSA-TS265, respectively (Fig. 1D and Supplementary material Table S1) confirming interaction. The number of TS265 molecules is higher for the BSA formulation when compared to HSA (Supplementary Table S3), correlating to a larger hydrodynamic diameter for the NanoTS265 (Supplementary material Table S1). Considering the higher loading capability of BSA, the subsequent studies were performed with this nanoformulation.

AuNP@PEG functionalization with Anti-EGFR and BSA originated AuNP@PEG@anti-EGFR_BSA that could be perceived by the traditional red-shift in plasmon absorption peak from 520 nm to 525 nm (Fig. 1C). In average, about 2 to 3 anti-EGFR molecules may be grafted to each AuNP. Anti-EGFR acts as targeting agent, and loading of TS265 onto this nanostructure yielded the TargetNanoTS265. A shift from 525 nm to 528 nm occurs when AuNP@PEG@anti-EGFR_BSA is functionalized with TS265 (Fig. 1E). Each Au-nanoconjugate carries in average 165 molecules of the TS265 compound. Functionalization with PTX was also achieved presenting a shift in plasmon absorption peak from 523 nm (AuNP@PEG@BSA) to 524 nm (AuNP@PEG@BSA@PTX - NanoPTX) (Supplementary material Fig. S3). This changes at the surface of AuNPs indicates the binding of PTX to the surface of the AuNP@PEG@BSA, in average 3000 to 4000 per AuNP for a hydrodynamic diameter of 410 ± 19 nm.

To evaluate the cytotoxicity of all nanoconjugates, three human cancer cell lines, A549, H1975, HCT116 were used exposed to the relative IC_{50} at 48 h. The IC_{50} of free TS265 in A549 and H1775 and of free PTX in HCT116 cell line were also calculated (at 48 h) (Supplementary material Fig. S4 and Fig. S5 and Table S4; and Ref [22] for HCT116). A decrease of the cell viability, in a dose-dependent manner, for both cell lines (A549 and H1975) (Supplementary Fig. S4) is clearly observed. TS265 is more active against colorectal carcinoma cells (HCT116) compared to lung adenocarcinoma cells (H1975 and A549) (IC_{50} = 0.206 compared to 0.349 μM and 0.741 μM, respectively) (Supplementary material Table S4). Lung adenocarcinoma cells with EGFR mutations are more susceptible to TS265 than Wild Type EGFR (A549) (IC_{50} = 0.349 μM compared to 0.741 μM) (Supplementary material Table S4). The three cell lines were incubated for 24 and 48 h in the presence of each nanoconjugates: AuNP@PEG, AuNP@PEG@BSA and AuNP@PEG@anti-EGFR_BSA (controls) and NanoTS265 and TargetNanoTS265 or the free TS265 at the respective IC_{50} for each cell line (Fig. 2). For comparison, the concentration of nanoconjugates used in all the assays has been calibrated to deliver the same amount of TS265 as the free compound concentration. Fig. 2 shows a strong reduction in cell viability for all three tumor cell lines when exposed to NanoTS265 and TargetNanoTS265 when compared to free compound (Table 1). The active targeted nanoconjugate (TargetNanoTS265) shows only a slightly higher cytotoxicity than the non-targeted counterpart after 24 h exposition in HCT116 and H1975 cells (Fig. 2). This slightly higher cytotoxicity at 24 h incubation correlates with the amount of internalized nanoconjugates in HCT116 cells (supplementary material Fig. S6).

Since nanoconjugates alone do not show any toxicity (Supplementary material Fig. S7), cell death ought to derive from the effect of the compound and, therefore, result in apoptosis as previously demonstrated for free TS265 [23] (Supplementary material Fig. S8).

To confirm selectivity of the nanoconjugates towards cancer cells, viability assays were also performed using primary normal human fibroblasts, using the IC_{50} of 0.206 μM, 0.349 μM and 0.741 μM for HCT116,

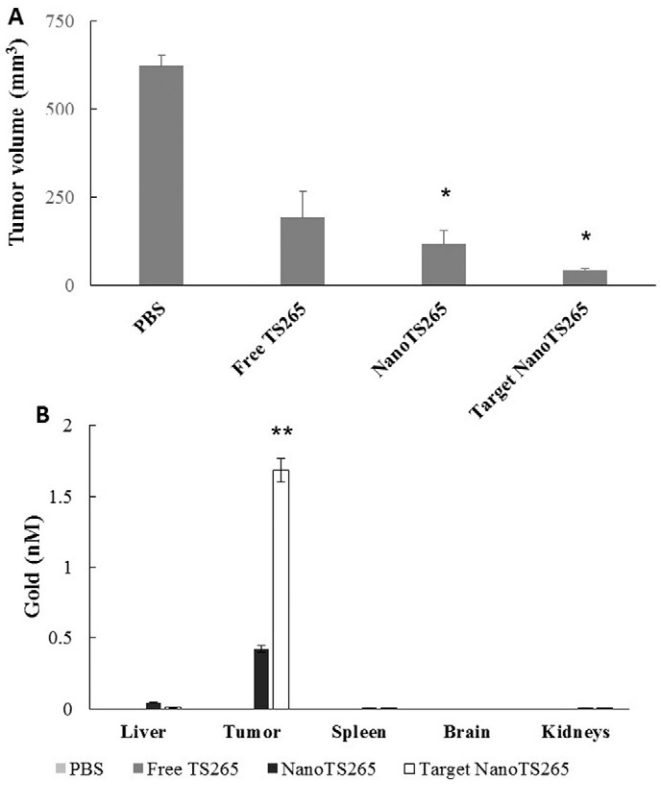

Fig. 6. A. Inhibition of tumor growth in NOD/scid mice treated with PBS, free TS265 and the NanoTS265 and TargetNanoTS265 nanoconjugates. Tumor burden was determined by the sum of tumor volumes per mouse ($n = 3$), in xenografted mice treated with PBS, the free TS265 or the nanoconjugates. All the results are expressed as the mean ± SEM. B. Concentration of gold (nM) based on ICP-MS in livers, spleens, brains, kidneys and tumors in NOD/scid mice treated with PBS, free TS265 and the NanoTS265 and TargetNanoTS265 nanoconjugates. $^{*}p < 0.01$ relative to PBS; $^{**}p < 0.005$ relative to PBS. Values represented were normalized to the mass of each organ.

H1975 and A549, respectively. Fig. 3 shows that nanoconjugates induce a significant reduction of cell viability of tumor cells in relation to normal fibroblasts. Considering that the compound itself already demonstrates considerable selectivity to cancer cells [25], the nanoformulations here depicted improve this selectivity by 50%, which per se might spare healthy tissues even for high doses.

Paclitaxel (PTX), free or in equivalent nanoformulations to those of TS265, was used to compare the efficacy of these nanoconjugates with a known chemotherapeutic drug. The IC_{50} of free PTX in HCT116 cell line were also determined (at 48 h) (Supplementary material Fig. S9 and Table S4), showing a decrease of HCT116 cell viability in a dose-dependent manner (Supplementary Fig. S9). When comparing both nanoconjugates, NanoTS265 and TargetNanoTS265 with NanoPTX (in respect to the free compound, Ts265 or PTX), it is evident that NanoTS265 formulations show higher cytotoxicity than NanoPTX (Fig. 4). NanoPTX showed no increase in cytotoxicity compared to free PTX.

Active targeting will deliver the chemotherapeutics to a specific cancer cell type whilst sparing the surrounding healthy tissue. As such, such effect is best observed when a given drug is administered to a mixture of cancer and healthy cells and the killing effect of the drug is more robustly observed for those active targeted, i.e. cancer cells. Thus, to corroborate that the higher efficacy of TargetNanoTS265 against cancer cells when compared to normal fibroblasts was due to the active targeting, we assessed the differential targeting of cancer cells by the nanoconjugates when in co-culture with healthy cells. To assess TargetNanoTS265 effective targeting mediated by EGFR, primary fibroblasts and HCT116 cancer cell line were plated in co-culture in a 1:1 ratio and, since fibroblasts express Vimentin and HCT116 tumor cells do not, it was possible to selectively stain these cell lines in co-culture to evaluate selective cytotoxicity. By measuring Corrected Total Cell Fluorescence (CTCF = integrated density − (cell area × mean fluorescence of background)), it is possible to differentiate the staining intensity with anti-Vimentin and phalloidin488 Alexafluor, and therefore assess targeting efficiency of the TargetNanoTS265. As selectivity towards cancer cells increase, staining of HCT116 decreases, influencing the overall intensity of phalloidin488; and HCT116 do not stain with vimentin. Fig. 5 shows that the ratio Vimentin/Phalloidin increases upon exposure to the nanoconjugates - 1.4 fold for NanoTS265 and a

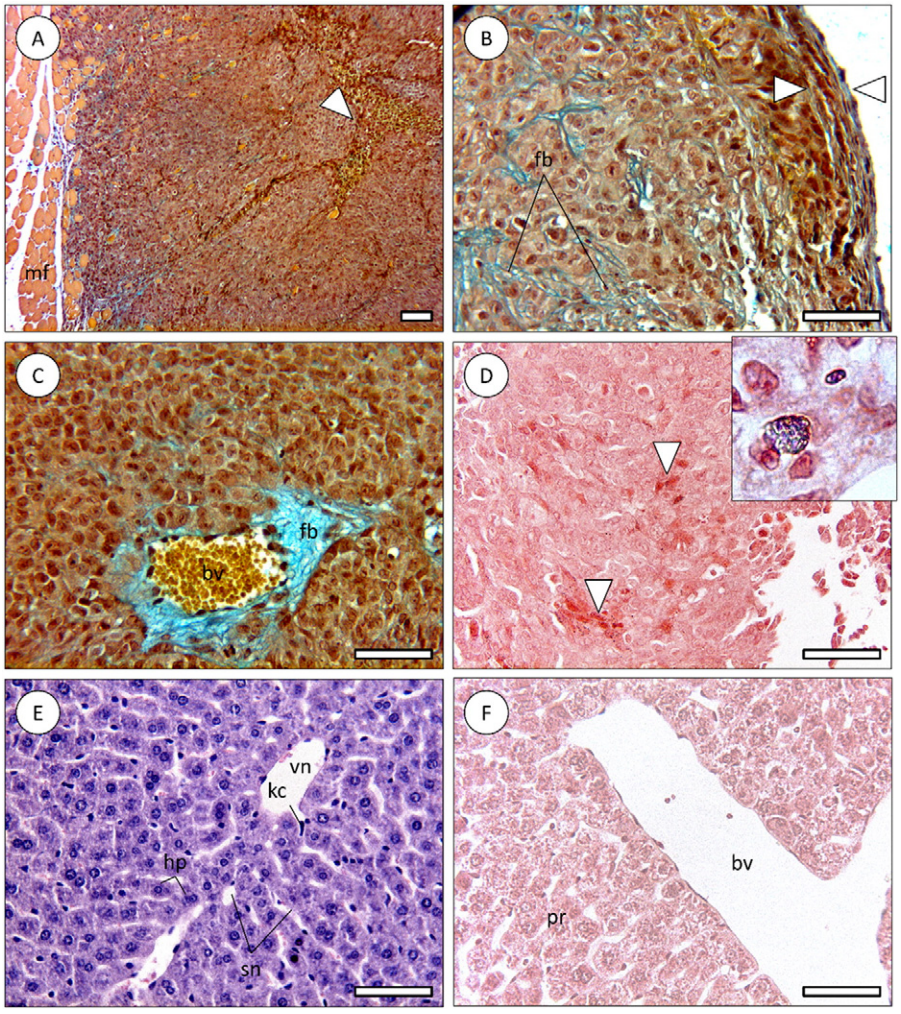

Fig. 7. Example micrographs of representative histological sections of subcutaneous tumor masses and liver of tested mice. A) Overview of a xenograft showing strong infiltration of inflammatory cells (arrowhead). The mass is intruding through subcutaneous muscle fibers (mf). B) Detail of the fibrotic encapsulation of the xenograft (between arrowheads). Unorganized non-elastic fibers (fb) were common near the edge of the mass, amidst tumor cells. C) An abnormal blood vessel (bv) with erythrocytes (but no inflammatory cells) inside the mass, lined with a dense layer of non-elastic fibers. D) Tumor mass revealing metallic deposits, especially n foci of infiltrating macrophages (arrowheads), further highlighted by stronger staining. Inset: Purplish metallic agglomerate inside a macrophage amidst the tumor mass, indicating the presence of fine gold deposits. E) Representative micrograph of the hepatic parenchyma of mice subjected to functionalized AuNPs, showing the normal architecture of the organ, namely regular-sized hepatocytes (hp) arranged in trabeculae. Many sinusoids (sn) branch from larger blood vessels such as the venule shown here (vn). kc) Kupffer cell. F) Micrograph of the liver of a mouse treated with functionalized AuPNs, exhibiting, as previous, no alterations to the hepatic parenchyma (pr) and no noticeable signs of metallic deposits. Note a hepatic portal blood vessel (bv) devoid of immune and holding scant erythrocytes, indicating absence of inflammatory processes. A–C, TC stain. D and F, Neutral Red. E, H&E. Scale bars: 100 μm (A) and 25 μm (B–F).

2.7 fold for TargetNanoTS265, thus confirming the targeting efficiency of TargetNanoTS265 towards EGFR in HCT116 cells.

Once the active targeting and anti-tumor potential of these gold nanoconjugates was demonstrated in vitro, we evaluated the in vivo efficacy on HCT116-derived xenografts induced by sub-cutaneous administration of 1×10^6 cells at the back hip of NOD/SCID mice. Tumors were allowed to grow until 1 mm^3 and treatments were initially performed with one i.v. tail injection with the free TS265 and the four nanoconjugates (AuNP@PEG, AuNP@PEG@BSA@PEG, NanoTS265 and TargetNanoTS265). A second dose of nanoconjugates was administered 4 days after the first injection. Five days after the second dose, mice were sacrificed and tumor, brain, spleen, kidneys and liver extracted and divided for ICP-MS and histology.

All TS265 formulations induced a reduction of tumor volume when compared to PBS control group: 69% for free TS265, 81% for NanoTS265 and 93% for TargetNanoTS265 (Fig. 6A). ICP-MS quantification showed the presence of gold in mice xenografts that were injected with NanoTS265 and TargetNanoTS265 (Fig. 6B). Moreover, the presence of gold was found mostly in the tumor samples and in much lower amounts in liver samples, no gold was detected in brain and a negligible amount in spleen and kidneys (Fig. 6B). Together, these data show a clear accumulation of the nanoformulations at the tumor site, either via an EPR or EPR associated to active targeting, which confirmed the targeted delivery of TS265 to the tumor via the gold nanoconjugates.

The subcutaneous tumors xenografts treated with NanoTS265 and TargetNanoTS265 were found to be solid and were formed by masses of anaplastic and neoplastic cells that formed distinct lobes, between which massive infiltration of inflammatory cells was always observed. The tumors were seemingly invasive of subcutaneous connective tissue and even of adjacent skeletal musculature, which is consistent with non-benign neoplasia (Fig. 7A). Related to the previous aspect, the tumors were only partially encapsulated by non-elastic (non-collagenous) fibers (Fig. 7B). Disorganized non-elastic fibers were consistently found among tumor cells, mainly near the margins of the xenografts. Blood vessels were sparse and presented an abnormal, irregular and highly fibrotic structure. Typically, these vessels did not contain leucocytes (Fig. 7C). Blackish metallic deposits were present in all tumor samples, inclusively in animals treated with free compound, albeit rare in control mice, from which the presence of Co-containing deposits may be inferred. The metallic deposits were seemingly more abundant and larger in macrophages than in tumor cells (Fig. 7D). Agglomerates of fine gold particles could be identified by its distinctive purplish tint in animals subjected to AuNPs (Fig. 7D, inset). As previously, these deposits were more common and larger in defense cells. No pathological traits were found in the livers of tested mice which invariably presented the normal mammalian architecture of the liver, consisting of regular hepatic cords lined by many sinusoids (Fig. 7E). No trace activation of the reticuloendothelial system (RES) was found, as well as significant evidence for NP agglomerates (Fig. 7F). Together these results show that these nanoconjugates are able to suppress tumor growth by 90% by selective accumulation in the tumor compared with to organs, with no signs of activation of innate immune response or of significant toxicological effects in the liver of tested mice.

10. Conclusion

The success of chemotherapy against cancer is strongly dependent on the controlled drug delivery to tumor cells while sparing the healthy tissues to the deleterious effects of most drugs. Recently, several platforms for the selective delivery of anti-cancer drugs have been proposed relying on the unique properties of nanoscale structures that may provide for enhanced efficacy against cancer. Here, we have demonstrated that an effective nanomedicine platform based on gold nanoparticles may be assembled with a simple architecture that is suitable for improved controlled delivery of metal complex drugs to cancer cells in a cell target fashion. We developed a AuNP complexed to PEG and a targeting moiety, in this case anti-EGFR to demonstrate the targeting potential and selectivity to cancer cells. BSA and HSA are abundant plasma proteins that can bind a variety of drugs impacting their delivery and efficacy, and modifying the drug's pharmacokinetic/pharmacodynamic properties. Their proposed role in drug delivery vehicles and systems, either alone or in association with other vectorization platforms, may influence targeting while decreasing side effects [28,29]. Thus, the use of BSA and/or HSA as carrier molecule of those chemicals showing to strongly interact with them, may be a powerful formulation to assist the assembly onto more robust and multifunctional platforms, such as nanoparticle to be used as a nanovectorization tool. In our case the easy conjugation of BSA to the AuNP@PEG@anti-EGFR may be used as loading vehicle for any anticancer drug that presents affinity to albumin. Considering this simple architecture, we demonstrated the full potential for carrying compounds with anti-proliferative potential in HCT116, A549 and H1975 cancer cell lines. As model we used PTX and TS265 (NanoTS265 and Target NanoTS265), one representative element of a larger family of metal complexes showing promising anti-cancer therapeutic capability.

Both the simple NanoTS265 and NanoPTX and the targeted counterparts were able to kill tumor cells in a selective manner with an efficiency of over 85%. When compared to the free compound, the nanoformulations were able to induce equivalent cell death to tumor cells with less than half the time of exposure, demonstrating that nanoconjugation was clearly beneficial to therapeutic outcome.

These nanoconjugates were further functionalized with anti-EGFR and showed remarkable selectivity towards cancer cells, which increased the delivery of the payload to tumor cells, thus improving efficacy. This effect was corroborated by the in vivo assays, which demonstrated that the simple nanoconjugates can suppress tumor growth by 60% that increase to 90% due to the active targeting provided by the antibody grafted to the surface.

This conceptual nanoconjugate design, due to the simplicity, may be easily tuned to fit other anticancer drugs and, depending on the required targeting moiety, other types of cancers. Several drug formulations in the clinics already profit from the conjugation to albumin as means to improve pharmacokinetics and drug efficacy, and we believe that the here presented nanoformulation may be small step in terms of formulation that provides for remarkable improvement to anti-tumor efficacy.

Acknowledgements

This work was supported by the Unidade de Ciências Biomoleculares Aplicadas – UCIBIO, financed by national funds from FCT/MEC (UID/Multi/04378/2013) and co-financed by the ERDF under the PT2020 Partnership Agreement (POCI-01-0145-FEDER-007728); PEst-OE/UID/DTP/04138/2013.

Appendix A. Supplementary data

Supplementary data to this article can be found online at http://dx.doi.org/10.1016/j.jconrel.2016.11.021.

References

[1] A. Wicki, D. Witzigmann, V. Balasubramanian, J. Huwyler, Nanomedicine in cancer therapy: challenges, opportunities, and clinical applications, J. Control. Release 200 (2015) 138–157.
[2] G. Bao, S. Mitragotri, S. Tong, Multifunctional nanoparticles for drug delivery and molecular imaging, Annu. Rev. Biomed. Eng. 15 (2013) 253–282.
[3] R.M. Cabral, P.V. Baptista, Anti-cancer precision theranostics: a focus on multifunctional gold nanoparticles, Expert. Rev. Mol. Diagn. 14 (2014) 1041–1052.
[4] C. Bao, J. Conde, E. Polo, P. del Pino, M. Moros, P.V. Baptista, V. Grazu, D. Cui, J.M. de la Fuente, A promising road with challenges: where are gold nanoparticles in translational research? Nanomedicine (Lond). 9 (2014) 2353–2370.
[5] D. Peer, J.M. Karp, S. Hong, O.C. Farokhzad, R. Margalit, R. Langer, Nanocarriers as an emerging platform for cancer therapy, Nat. Nanotechnol. 2 (2007) 751–760.

[6] I.A. Khawar, J.H. Kim, H.J. Kuh, Improving drug delivery to solid tumors: priming the tumor microenvironment, J. Control. Release 201 (2015) 78–89.
[7] E. Pérez-Herrero, A. Fernández-Medarde, Advanced targeted therapies in cancer: drug nanocarriers, the future of chemotherapy, Eur. J. Pharm. Biopharm. 93 (2015) 52–79.
[8] E.C. Dreaden, L.A. Austin, M.A. Mackey, M.A. El-Sayed, Size matters: gold nanoparticles in targeted cancer drug delivery, Ther. Deliv. 3 (2012) 457–478.
[9] J. Conde, A. Ambrosone, V. Sanz, Y. Hernandez, V. Marchesano, F. Tian, H. Child, C.C. Berry, M.R. Ibarra, P.V. Baptista, et al., Design of multifunctional gold nanoparticles for in vitro and in vivo gene silencing, ACS Nano 6 (2012) 8316–8324.
[10] G. Lin, P. Mi, C. Chu, J. Zhang, G. Liu, Inorganic nanocarriers overcoming multidrug resistance for cancer theranostics, Adv. Sci. (2016), http://dx.doi.org/10.1002/advs.201600134.
[11] J. Conde, J. Rosa, J.M. de la Fuente, P.V. Baptista, Gold-nanobeacons for simultaneous gene specific silencing and intracellular tracking of the silencing events, Biomaterials 34 (2013) 2516–2523.
[12] J. Conde, M. Larguinho, A. Cordeiro, L.R. Raposo, P.M. Costa, S. Santos, M.S. Diniz, A.R. Fernandes, P.V. Baptista, Gold-nanobeacons for gene therapy: evaluation of genotoxicity, cell toxicity and proteome profiling analysis, Nanotoxicology 8 (2014) 521–532.
[13] J. Conde, N. Oliva, N. Artzi, Implantable hydrogel embedded dark-gold nanoswitch as a theranostic probe to sense and overcome cancer multidrug resistance, Proc. Natl. Acad. Sci. U. S. A. 112 (2015) E1278–E1287.
[14] V.P. Torchilin, R. Rammohan, V. Weissig, T.S. Levchenko, TAT peptide on the surface of liposomes affords their efficient intracellular delivery even at low temperature and in the presence of metabolic inhibitors, Proc. Natl. Acad. Sci. U. S. A. 98 (2001) 8786–8791.
[15] A. Kumar, H. Ma, X. Zhang, K. Huang, S. Jin, J. Liu, T. Wei, W. Cao, G. Zou, X.J. Liang, Gold nanoparticles functionalized with therapeutic and targeted peptides for cancer treatment, Biomaterials 33 (2012) 1180–1189.
[16] M.K. Yu, J. Park, S. Jon, Targeting strategies for multifunctional nanoparticles in cancer imaging and therapy, Theranostics 2 (2012) 3–44.
[17] C.M. Beddoes, C.P. Case, W.H. Briscoe, Understanding nanoparticle cellular entry: a physicochemical perspective, Adv. Colloid Interf. Sci. 218 (2015) 48–68.
[18] S.T. Stern, P.P. Adiseshaiah, R.M. Crist, Autophagy and lysosomal dysfunction as emerging mechanisms of nanomaterial toxicity, Part. Fibre Toxicol. 9 (2012) 20.
[19] J. Spadavecchia, D. Movia, C. Moore, C.M. Maguire, H. Moustaoui, S. Casale, Y. Volkov, A. Prina-Mello, Targeted polyethylene glycol gold nanoparticles for the treatment of pancreatic cancer: from synthesis to proof-of-concept in vitro studies, Int. J. Nanomedicine 11 (2016) 791–822.
[20] A. Waheed, A. Gupta, P. Patel, Targeted drug delivery systems for pancreatic cancer, PharmaTutor Mag. 3 (2015) 3462–3482.
[21] R. Mendes, B. Carreira, P.V. Baptista, A.R. Fernandes, Non-small cell lung cancer biomarkers and targeted therapy - two faces of the same coin fostered by nanotechnology, Expert Ver. Precis. Med. Drug Dev. 1 (2016) 155–168.
[22] T.F.S. Silva, P. Smoleński, L.M.D.R.S. Martins, M.F.C. Guedes da Silva, A.R. Fernandes, D. Luis, A. Silva, S. Santos, P.M. Borralho, C.M.P. Rodrigues, et al., Cobalt and zinc compounds bearing 1,10-phenanthroline-5,6-dione or 1,3,5-triaza-7-phosphaadamantane derivatives - synthesis, characterization, cytotoxicity, and cell selectivity studies, Eur. J. Inorg. Chem. 2013 (2013) 3651–3658.
[23] A. Silva, D. Luis, S. Santos, J. Silva, A.S. Mendo, L. Coito, T.F. Silva, M.F. da Silva, L.M. Martins, A.J. Pombeiro, P.M. Borralho, C.M. Rodrigues, M.G. Cabral, P.A. Videira, C. Monteiro, A.R. Fernandes, Biological characterization of the antiproliferative potential of Co(II) and Sn(IV) coordination compounds in human cancer cell lines: a comparative proteomic approach, Drug Metabol. Drug Interact. 28 (2013) 167–176.
[24] D.V. Luís, J. Silva, A.I. Tomaz, R.F.M. de Almeida, M. Larguinho, P.V. Baptista, L.M.D.R.S. Martins, T.F.S. Silva, P.M. Borralho, C.M.P. Rodrigues, A.S. Rodrigues, A.J. Pombeiro, A.R. Fernandes, Insights into the mechanisms underlying the anti-proliferative potential of a Co(II) coordination compound bearing 1,10-phenanthroline-5,6-dione: DNA and protein interaction studies, J. Biol. Inorg. Chem. 19 (2014) 787–803.
[25] C. Lee, D. Meisel, Adsorption and surface-enhanced Raman of dyes on silver and gold sols, J. Phys. Chem. 86 (1982) 3391–3395.
[26] P.M. Costa, M.H. Costa, Development and application of a novel histological multichrome technique for clam histopathology, J. Invertebr. Pathol. 110 (2012) 411–414.
[27] Y. Li, W.Y. He, J.Q. Liu, F.L. Sheng, Z.D. Hu, X.G. Chen, Biochim. Biophys. Acta 1722 (2005) 15–21.
[28] F. Yang, Y. Zhang, H. Liang, Interactive association of drugs binding to human serum albumin, Int. J. Mol. Sci. 15 (2014) 3580–3595.
[29] S. Bi, Y. Sunb, C. Qiao, H. Zhang, C. Liu, Binding of several anti-tumor drugs to bovine serum albumin: fluorescence study, J. Lumin. 129 (2009) 541–547.